PNAS

Supporting Information for

Ferromagnetic ordering correlated strong metal-oxygen hybridization for superior oxygen reduction reaction activity

Jisi Li, Caiyan Zheng, Erling Zhao, Jing Mao, Yahui Cheng, Hui Liu, Zhenpeng Hu, Tao Ling

Tao Ling, Zhenpeng Hu, Hui Liu.
Email: lingt04@tju.edu.cn; zphu@nankai.edu.cn; hui_liu@tju.edu.cn

This PDF file includes:

Supporting Information Text

Note S1. Determination of the site densities of Mn ions on FM-$Mn_2V_2O_7$ and AFM-MnV_2O_6 by CV fitting method

The real-time evolution of surface Mn ions on FM-$Mn_2V_2O_7$ and AFM-MnV_2O_6 were monitored by quantitative CV analysis. As shown in Fig. 3*A*, FM-$Mn_2V_2O_7$ and AFM-MnV_2O_6 exhibit quite different electrochemical behaviours with varying potentials and shapes of the oxidative and reductive peaks. In order to effectively separate these redox peaks, cubic spline interpolation method was firstly used to obtain and separate the double layer currents (Fig. S8). Fitting analysis was further conducted to identify the oxidation and reduction peaks in the separated curves (Fig. S9). To obtain a general peak function for the redox reactions in the CV curves, the Nernst equation was modified by introducing the apparent number of transferred electrons (*n*') and peak centre (E_{peak}). The modified Nernst function is shown as following:

$$j = \frac{n'^2 v \Gamma_S \frac{F^2}{RT} exp\left[\frac{n'F}{RT}(E-E_{peak})\right]}{\left\{exp\left[\frac{n'F}{RT}(E-E_{peak})\right]+1\right\}^2} \quad (S1)$$

where *j* is the current density, *v* is the scan rate, Γ_S is the surface site concentration, *F* is Faraday constant (96485 C mol^{-1}), *R* is the ideal gas constant (8.314 J mol^{-1} K^{-1}), *T* is the absolute temperature, and *E* is the electrode potential. Fityk program embedded with the modified Nernst function was performed to fit the separated CV curves. As shown in Fig. S9, three anodic peaks centred at 0.65, 0.92 and 1.01 V_{RHE} were evident, which should be assigned to Mn^{2+}→Mn_3O_4, Mn^{2+}→Mn^{3+} and Mn^{2+}/Mn^{3+}→Mn^{4+}, respectively, according to the reported Pourbaix diagram of Mn oxides (1, 2). The site densities of Mn^{2+}, Mn^{3+} and Mn^{4+} on FM-$Mn_2V_2O_7$ and AFM-MnV_2O_6 can be obtained by extracting Γ_S from the corresponding peaks in the CV curves. The results were provided in Table S2.

In order to verify the accuracy of our quantitative CV method for *in situ* analysis of the site densities of Mn ions, FM-$Mn_2V_2O_7$ and AFM-MnV_2O_6 were characterized by *ex situ* X-ray photoelectron spectroscopy (XPS) after testing at 1.20 V_{RHE} (Fig. S12). As shown in Table S3, the number ratios of Mn^{3+} and Mn^{4+} in FM-$Mn_2V_2O_7$ and AFM-MnV_2O_6 obtained by XPS are similar to those by CV analysis.

Note S2. $Mn_2V_2O_7$ with other AFM orderings

In the main text, the AFM ordering of $Mn_2V_2O_7$ (AFM-$Mn_2V_2O_7$), that is, the nearest Mn atoms inside the same [MnO_6] layer are arranged alternately with opposite spins, was selected to effectively illustrate the effect of AFM interaction on ORR thermodynamics. Besides, an interlayer AFM ordered $Mn_2V_2O_7$ model (Fig. S18, *A* and *B*), in which the Mn atoms exhibit opposite spins in the neighboring [MnO_6] layers but parallel spins inside the same [MnO_6] layer (hereafter, this structure was referred to as AFM-interlayer $Mn_2V_2O_7$), was constructed. Other AFM arrangements were not considered because of their higher energy than AFM-interlayer $Mn_2V_2O_7$. It is found that the energy of AFM-interlayer $Mn_2V_2O_7$ is slightly higher than that of the FM-$Mn_2V_2O_7$ and lower than that of the AFM-$Mn_2V_2O_7$ (Table S7). This result is reasonable that previous work (1) has demonstrated that the spins on Mn atoms in $Mn_2V_2O_7$ favor FM interactions within the same [MnO_6] layer and the interlayer magnetic coupling between the neighbouring [MnO_6] layers is rather weak because of their separation by the non-magnetic [VO_n] layer.

Note S3. Construction of $Mn_2V_2O_7$ surface for calculations

According to the literature (3), the surface of oxide electrocatalyst is easily covered by *OH at the onset potential of ORR. Therefore, a *OH covered $Mn_2V_2O_7$ (001) surface was constructed (Fig. 4*A*, Figs. S16 and S17). Bader charge of the surface Mn atoms on $Mn_2V_2O_7$ surface was analysed, and bulk MnO, Mn_3O_4, Mn_2O_3 and MnO_2 were introduced as references. As shown in Table S8, the calculated Bader charge of Mn site on the surface of $Mn_2V_2O_7$ is −1.745 |e|, which is very close to the value of Mn site on Mn_2O_3. This result demonstrates that the valence state of Mn site on $Mn_2V_2O_7$ surface is close to +3, which is consistent with the experimentally observed results from CV and XANES that large amounts of Mn^{3+} generated on FM-$Mn_2V_2O_7$.

Note S4. Evaluation of specific activities (i_s) of FM-$Mn_2V_2O_7$ and Pt/C

To carefully assess the ORR intrinsic activity of FM-$Mn_2V_2O_7$, we measured the electrochemical surface area (ECSA) of FM-$Mn_2V_2O_7$ following the classical double layer capacitance method (4). As shown in Fig. S23*A*, the ECSA of FM-$Mn_2V_2O_7$ was 17.7 m^2 g^{-1}, which is very close to the Brunauer-Emmett-Teller (BET) surface area of the structural templates of FM-$Mn_2V_2O_7$ (24.12 m^2 g^{-1}). Here, the specific activity of FM-$Mn_2V_2O_7$ was obtained by normalizing its kinetic current with respect to the BET surface area. For Pt/C catalyst, the specific surface area was estimated by hydrogen underpotential deposition method (5) (Fig. S23*B*, 51.7 m^2 g^{-1}).

Note S5. The structural stability of FM-$Mn_2V_2O_7$

The FM-$Mn_2V_2O_7$ catalyst maintains its crystal structure during the ORR process (Fig. S24) despite a significant change in the valence state of surface Mn ions (Fig. S12). This structural stability can be attributed to the presence of V^{5+} sites. Specifically, V^{5+} is rich in empty *d* orbitals, which acts as an "electron sponge" that can accept/donate a large number of electrons from/to active [MnO_6] units under reaction conditions, thereby helping to maintain overall structural stability of the catalyst. As a result, FM-$Mn_2V_2O_7$ exhibits an excellent durability (Fig. S20).

Supplementary Figures

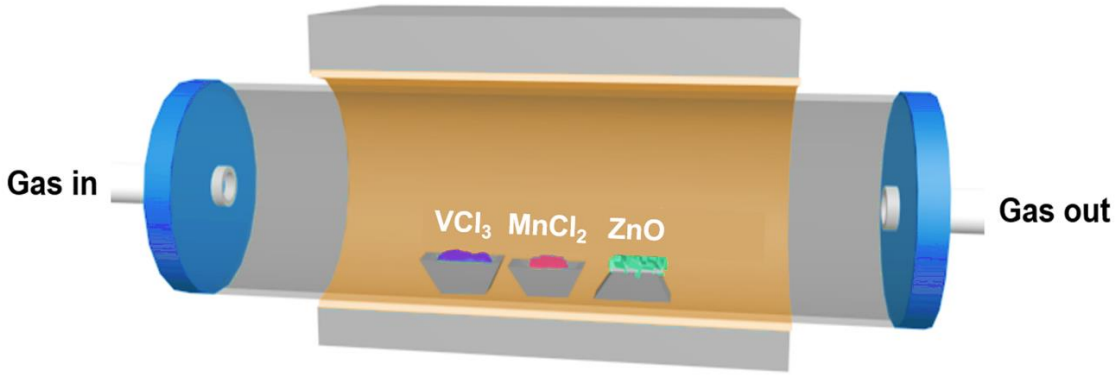

Fig. S1. Schematic diagram of the experimental apparatus for the cation exchange method in this work. Note that the ZnO templates were placed in the center of the tube, and $MnCl_2$ and VCl_3 powders were placed 4.5 and 9.5 cm upstream of the tube center, respectively.

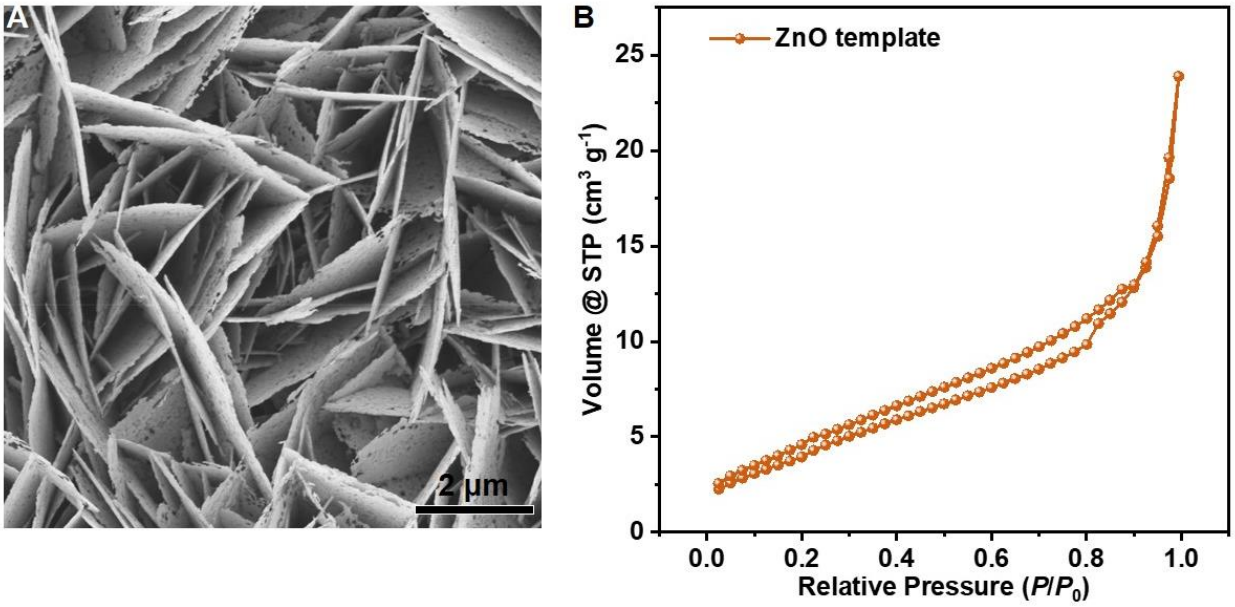

Fig. S2. Characterization of ZnO templates. A, SEM image. **B**, Nitrogen physisorption isotherms. The measured BET surface area of the ZnO templates is 16.05 m^2 g^{-1}. Note that FM-$Mn_2V_2O_7$ and AFM-MnV_2O_6 were converted from ZnO templates by a cation exchange method, in which the morphology of the templates was preserved. Therefore, the three materials should possess similar surface areas.

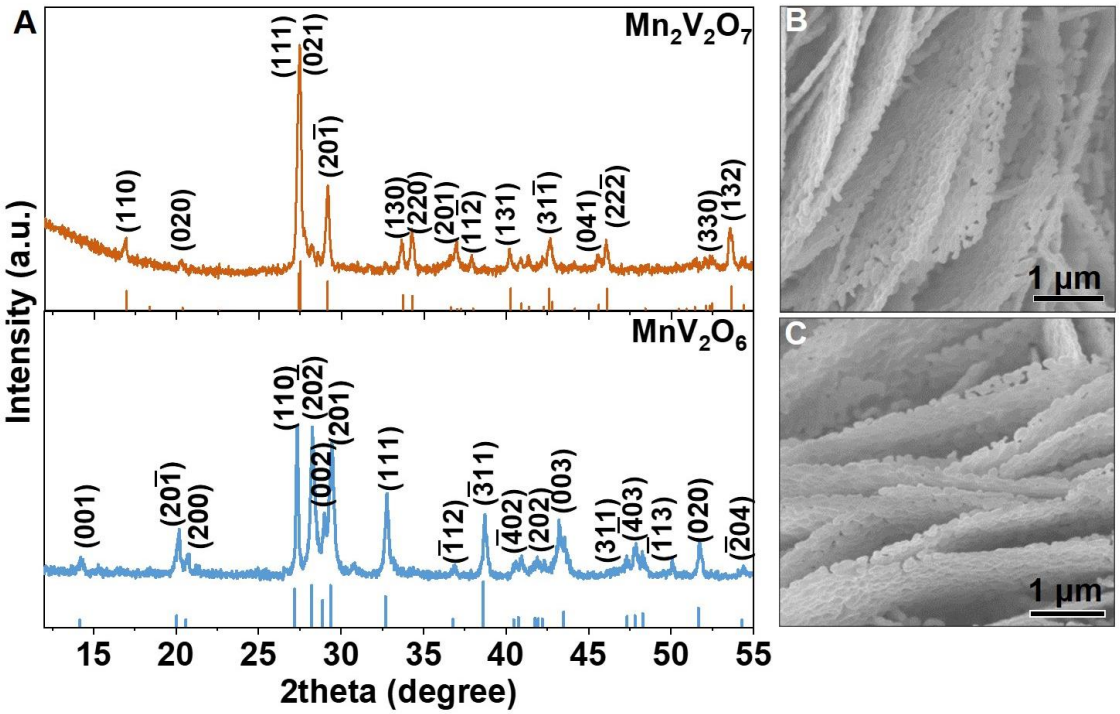

Fig. S3. Characterizations of FM-$Mn_2V_2O_7$ and AFM-MnV_2O_6. A, XRD patterns of FM-$Mn_2V_2O_7$ and AFM-MnV_2O_6. **B**, SEM image of FM-$Mn_2V_2O_7$. **C**, SEM image of AFM-MnV_2O_6. As shown, FM-$Mn_2V_2O_7$ and AFM-MnV_2O_6 exhibit very similar morphology as the ZnO templates (Fig. S2*A*).

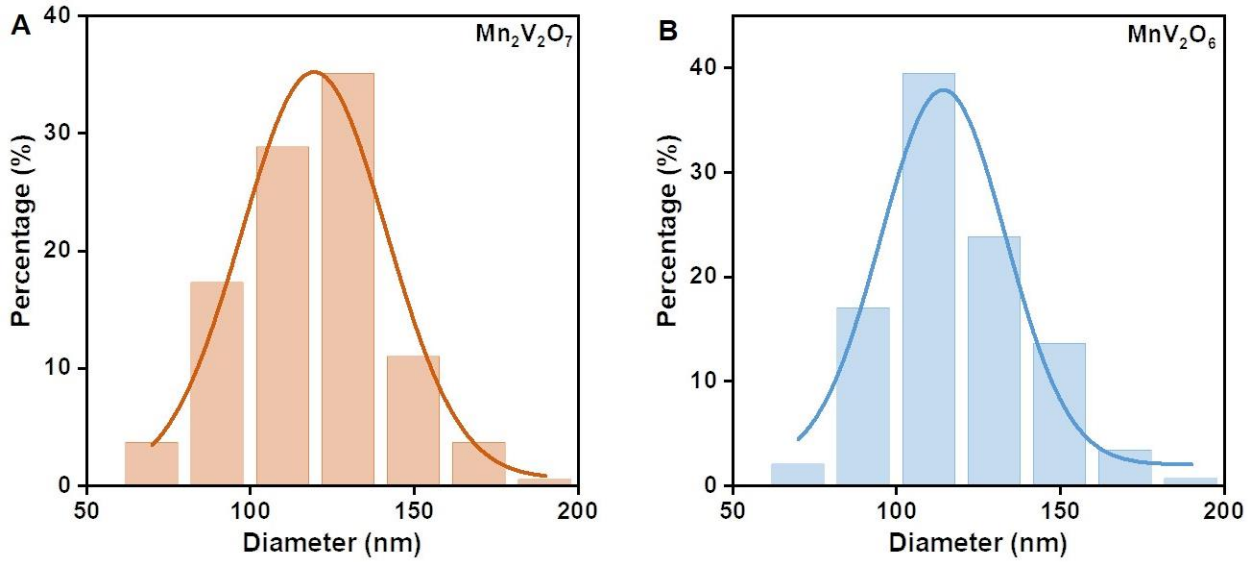

Fig. S4. Particle size distributions of FM-$Mn_2V_2O_7$ and AFM-MnV_2O_6 based on SEM characterizations. **A**, FM-$Mn_2V_2O_7$. **B**, AFM-MnV_2O_6. As shown, the size distributions of FM-$Mn_2V_2O_7$ and AFM-MnV_2O_6 were similar, ranging from 50 to 200 nm.

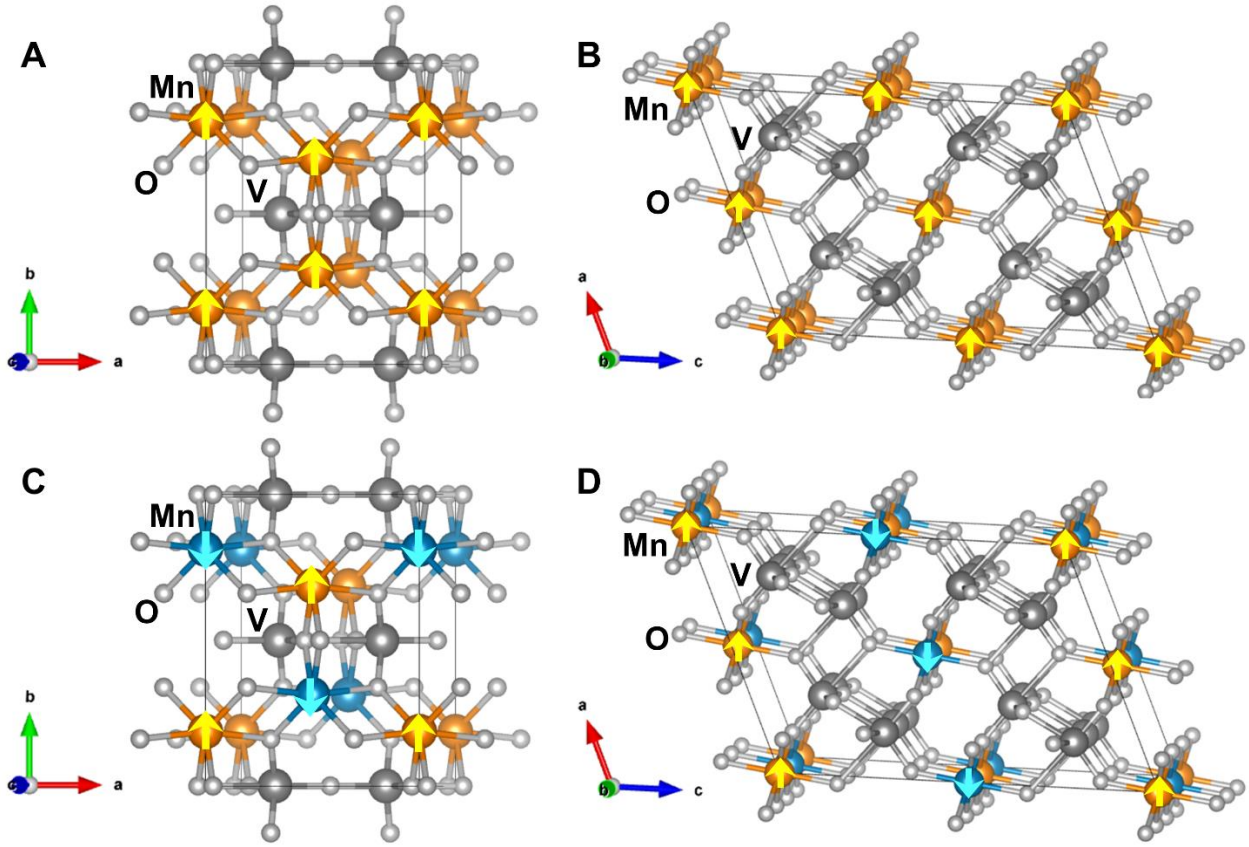

Fig. S5. Calculation models of bulk $Mn_2V_2O_7$ and MnV_2O_6. A and **C**, $Mn_2V_2O_7$ with ferromagnetic (FM) and antiferromagnetic (AFM) orderings, respectively (a = 6.54 Å, b = 8.97 Å, c = 5.09 Å, $\alpha = \gamma = 90.00°$, β = 102.13°). **B** and **D**, MnV_2O_6 with FM and AFM orderings, respectively (a = 9.45 Å, b = 7.17 Å, c = 13.68 Å, $\alpha = \gamma = 90.00°$, β = 113.31°).

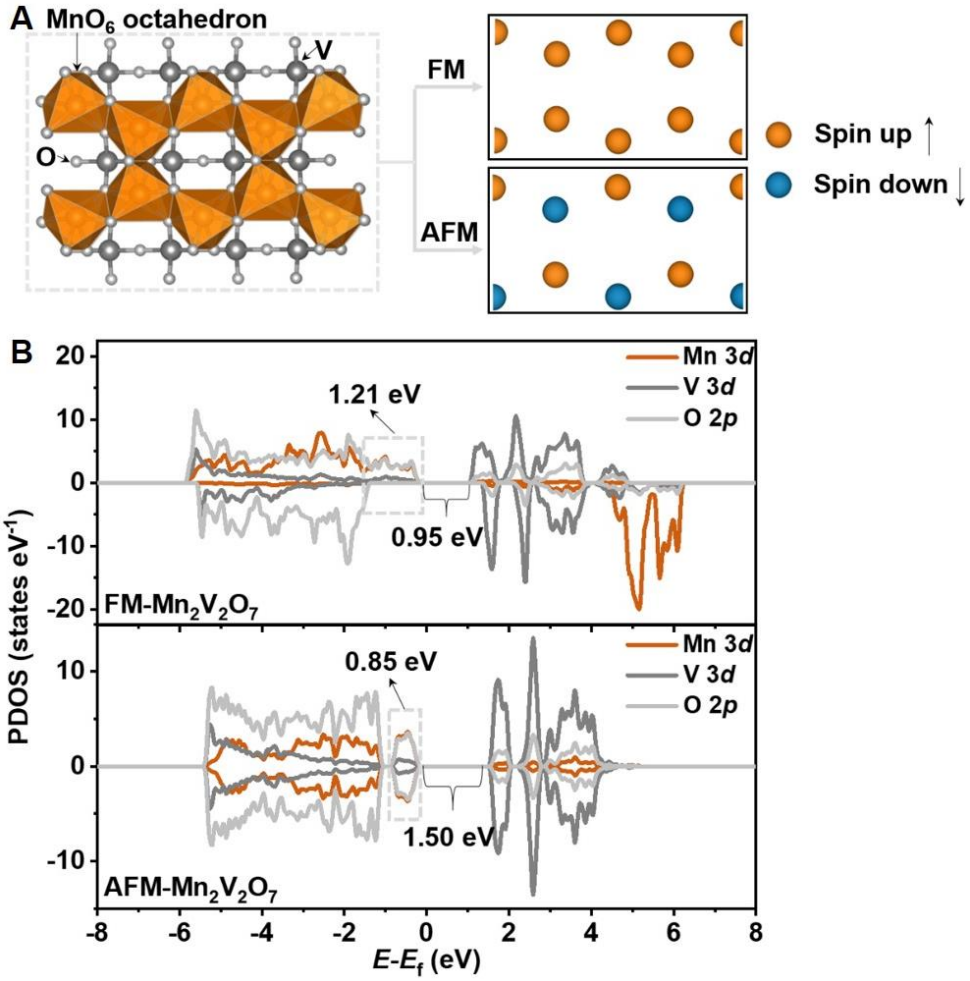

Fig. S6. Spin isosurfaces and PDOS of $Mn_2V_2O_7$ with FM and AFM orderings. A, Spin isosurfaces of $Mn_2V_2O_7$ (001) plane with FM and AFM orderings. **B**, PDOS of $Mn_2V_2O_7$ with FM and AFM orderings. As shown in **B**, the electronic structure of $Mn_2V_2O_7$ is significantly affected by its magnetic ordering. First, Mn-3*d* orbitals of FM-$Mn_2V_2O_7$ overlap strongly with its O-2*p* orbitals near the Fermi level. Second, FM-$Mn_2V_2O_7$ exhibits a band broadening (~1.21 eV) near the Fermi level compared to that in AFM-$Mn_2V_2O_7$ (~0.85 eV). This indicates more delocalized electronic states of FM-$Mn_2V_2O_7$, which would decrease the energetic cost to accept/donate electrons at the adsorbate-catalyst interface (6). Third, the band gap of FM-$Mn_2V_2O_7$ is reduced by 0.55 eV compared with that of AFM-$Mn_2V_2O_7$, demonstrating more favorable charge transport inside the catalyst.

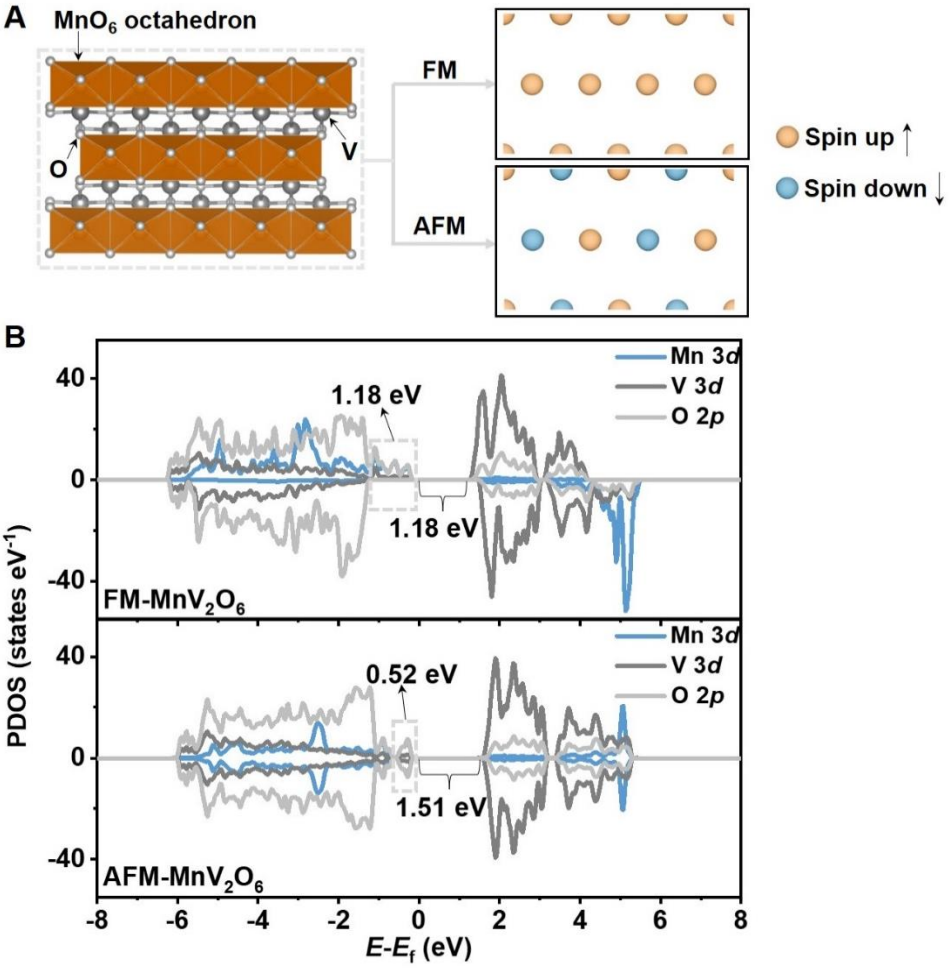

Fig. S7. Spin isosurfaces and PDOS of MnV_2O_6 with FM and AFM orderings. A, Spin isosurfaces of MnV_2O_6 (001) plane with FM and AFM orderings. **B**, PDOS of MnV_2O_6 with FM and AFM orderings. Similar as $Mn_2V_2O_7$, Mn-3*d* orbitals of FM-MnV_2O_6 overlap strongly with its O-2*p* orbitals near the Fermi level. In addition, FM-MnV_2O_6 exhibits a band broadening (~1.18 eV) near the Fermi level compared to that in AFM-MnV_2O_6 (~0.52 eV). Moreover, the band gap of FM-MnV_2O_6 is reduced by 0.33 eV compared with that of AFM-MnV_2O_6.

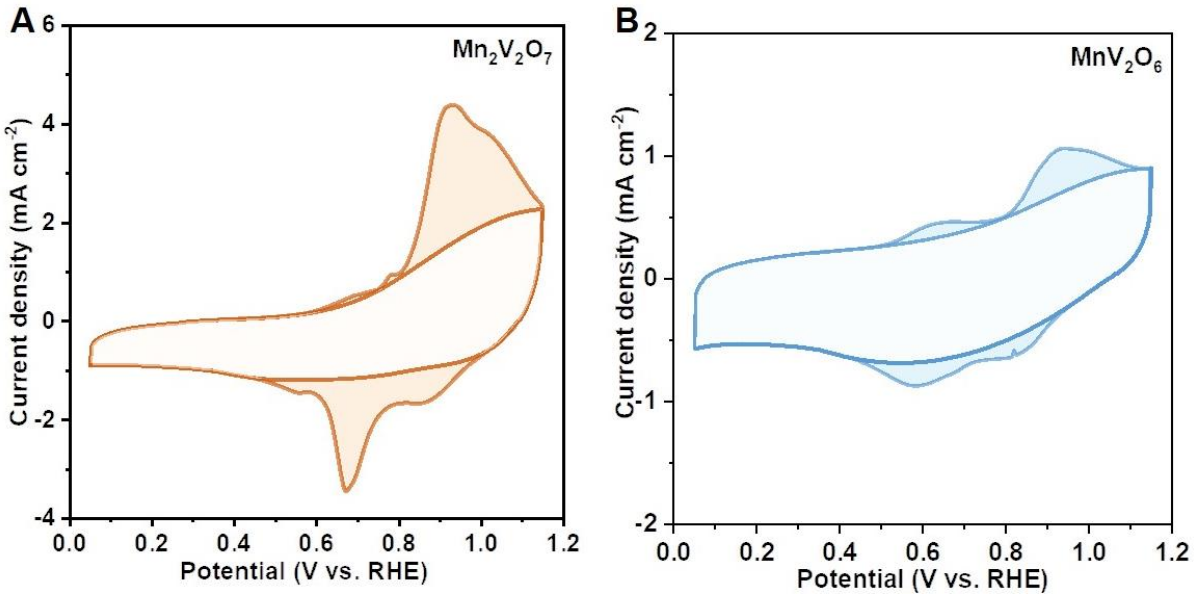

Fig. S8. CV curves of FM-$Mn_2V_2O_7$ and AFM-MnV_2O_6. A, FM-$Mn_2V_2O_7$. **B**, AFM-MnV_2O_6. The shadow areas in **A** and **B** are the separated oxidation and reduction peaks for the oxides.

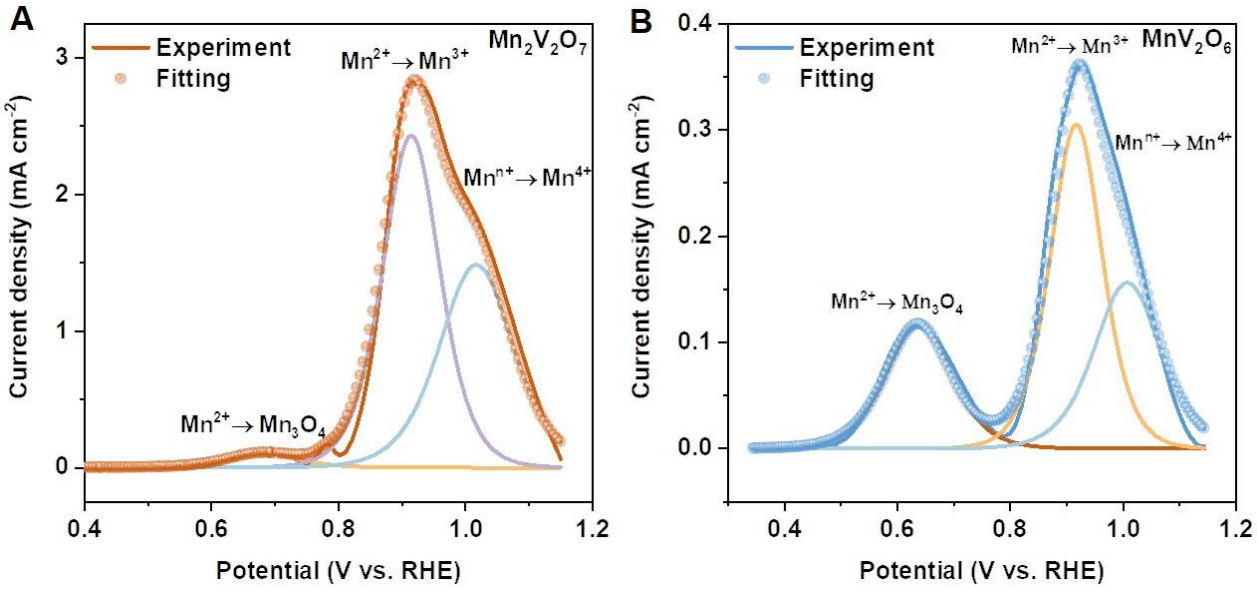

Fig. S9. Fitting of the anodic peaks in the separated CV curves of FM-$Mn_2V_2O_7$ and AFM-MnV_2O_6. A, FM-$Mn_2V_2O_7$. **B**, AFM-MnV_2O_6. Note that Mn^{n+} denotes Mn^{2+} or Mn^{3+} species. The fitting results were provided in Table S2.

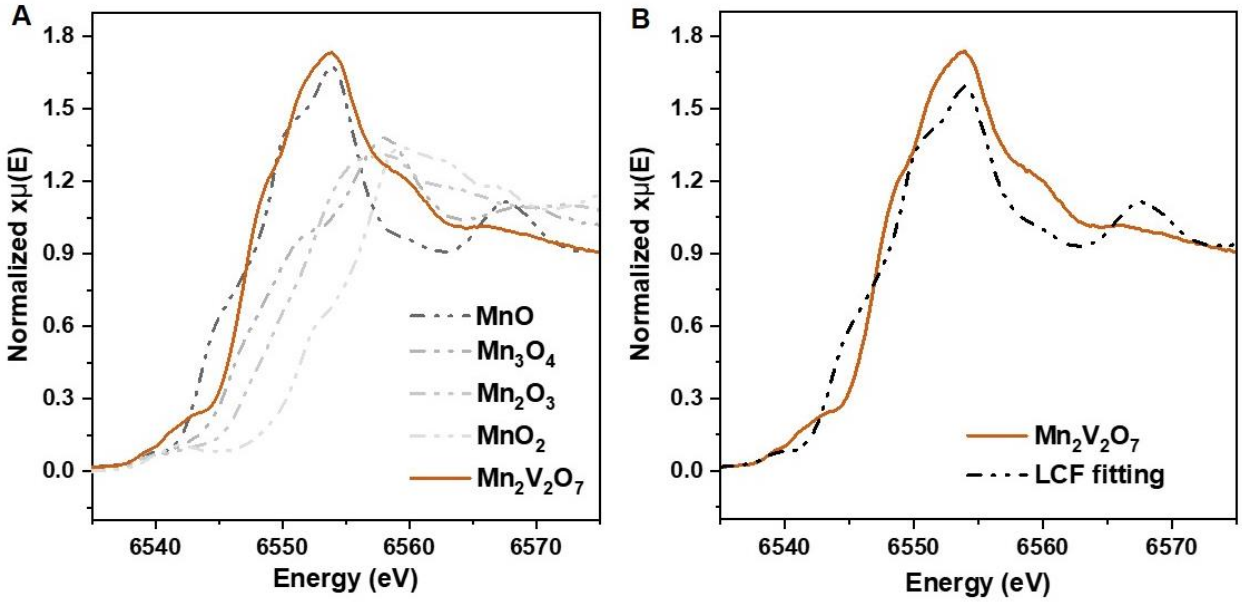

Fig. S10. Analysis of Mn valence state of FM-$Mn_2V_2O_7$. A, Mn *K*-edge XANES spectra of $Mn_2V_2O_7$, MnO, Mn_3O_4, Mn_2O_3 and MnO_2. **B**, Fitting result of $Mn_2V_2O_7$ by linear combination fitting (LCF) method (7). The fitting result was provided in Table S4.

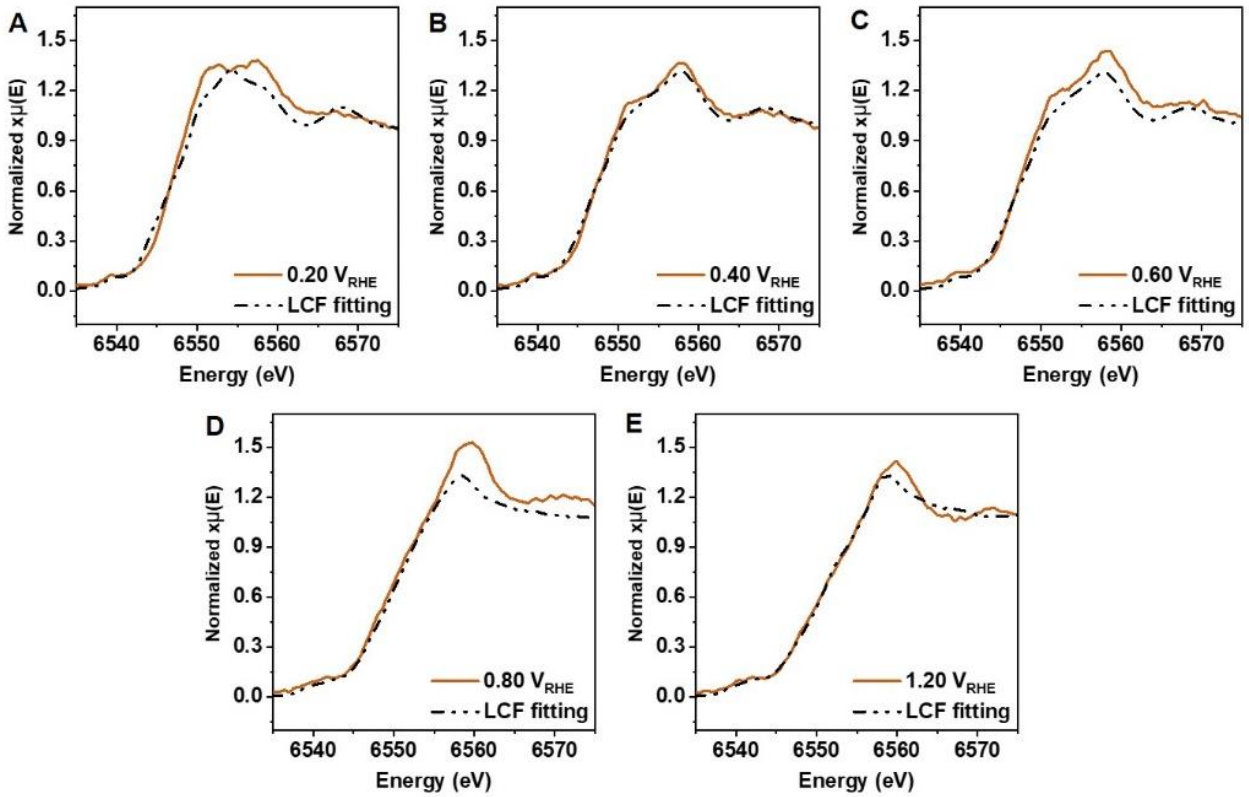

Fig. S11. Analysis of Mn valence state of FM-$Mn_2V_2O_7$ at different applied potentials. A-E, *In situ* Mn *K*-edge XANES spectra and corresponding LCF fitting results of FM-$Mn_2V_2O_7$ at 0.20, 0.40, 0.60, 0.80 and 1.20 V_{RHE}, respectively. The fitting results were provided in Table S4.

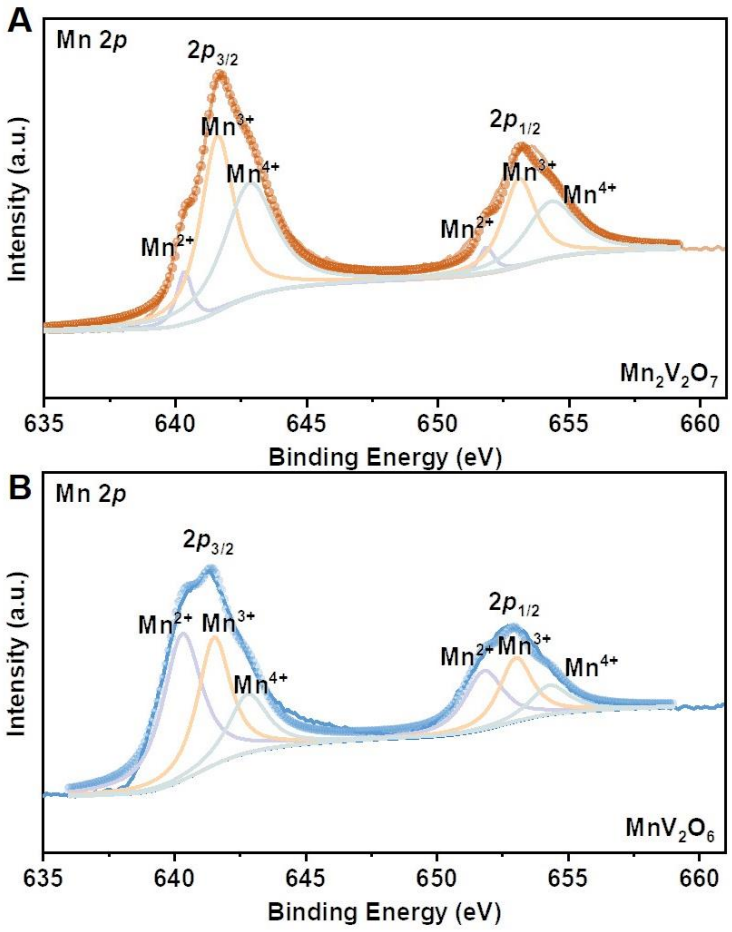

Fig. S12. XPS spectra of FM-$Mn_2V_2O_7$ and AFM-MnV_2O_6 after testing at 1.20 V_{RHE}. A, FM-$Mn_2V_2O_7$. **B**, AFM-MnV_2O_6. The relative contents of Mn^{2+}/Mn^{3+}/Mn^{4+} and average valence states were provided in Table S5.

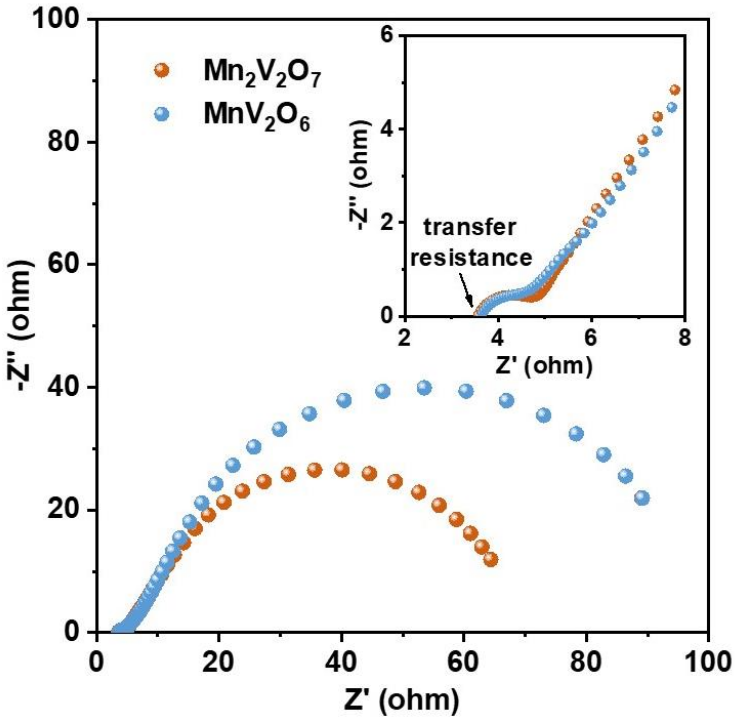

Fig. S13. EIS spectra of FM-$Mn_2V_2O_7$ and AFM-MnV_2O_6 at 0.85 V_{RHE} collected from 100 kHz to 0.1 Hz.

In our CV and LSV tests, the $Mn_2V_2O_7$ and MnV_2O_6 catalysts were mixed with highly-conductive carbon black to eliminate differences in electronic conductivity within the electrodes (8, 9). As seen, the prepared $Mn_2V_2O_7$ and MnV_2O_6 electrodes have similar transfer resistance (mainly associated with the electron transfer in the catalysts and the ion transfer in the electrolyte). Therefore, the increased oxidation of Mn^{2+} to Mn^{3+} in FM-$Mn_2V_2O_7$ can be attributed to the enhanced Mn-O hybridization, rather than the intrinsic high electrical conductivity of FM-$Mn_2V_2O_7$.

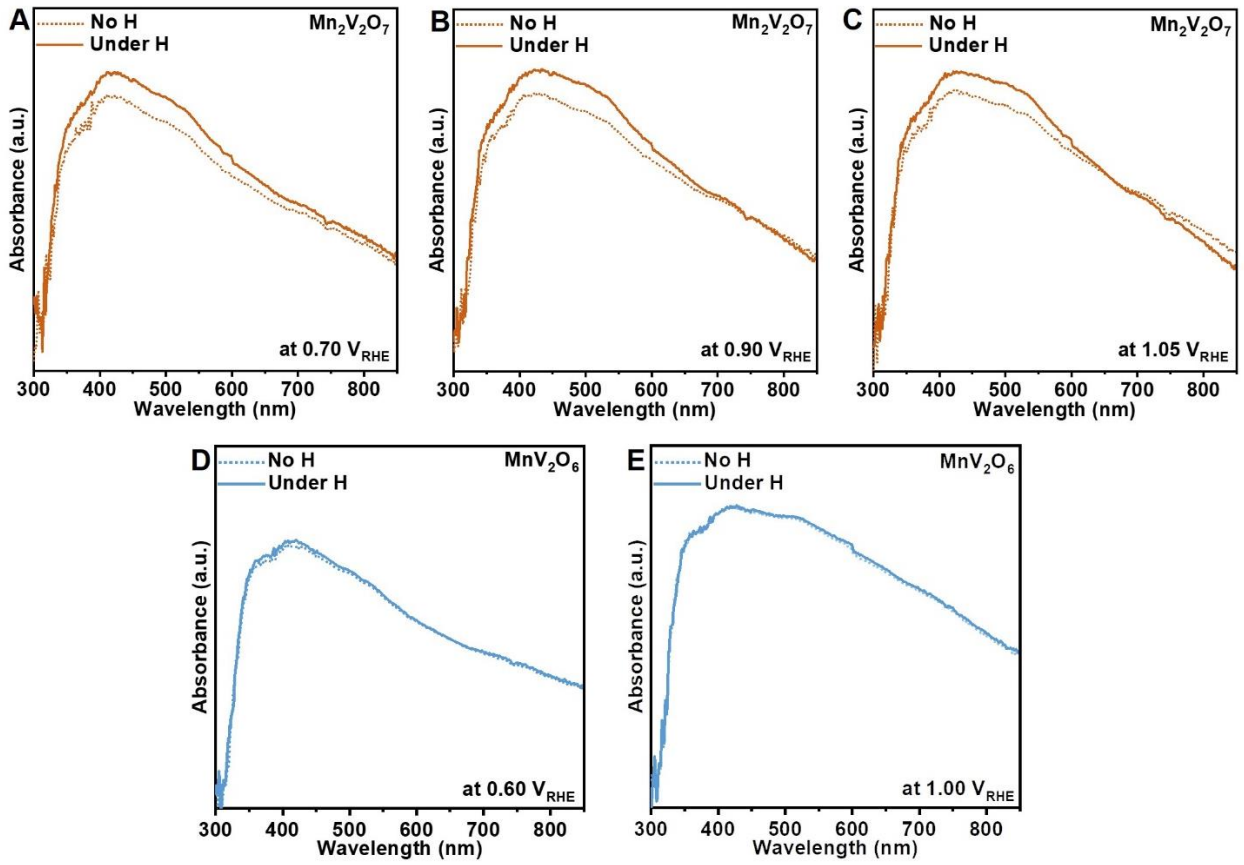

Fig. S14. *In situ* UV-Vis spectra of FM-$Mn_2V_2O_7$ and AFM-MnV_2O_6 at different applied potentials. A-**C**, *In situ* UV-Vis spectra of $Mn_2V_2O_7$ at 0.70, 0.90 and 1.05 V_{RHE}, respectively. **D** and **E**, *In situ* UV-Vis spectra of MnV_2O_6 at 0.60 and 1.00 V_{RHE}, respectively.

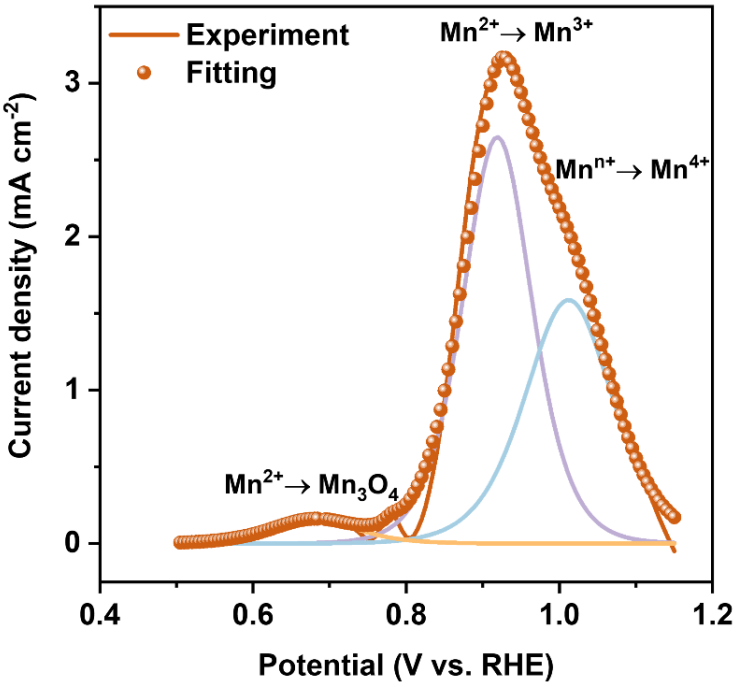

Fig. S15. Fitting of anodic peaks in the separated CV curve of FM-$Mn_2V_2O_7$ under magnetic field. The fitting result was provided in Table S2.

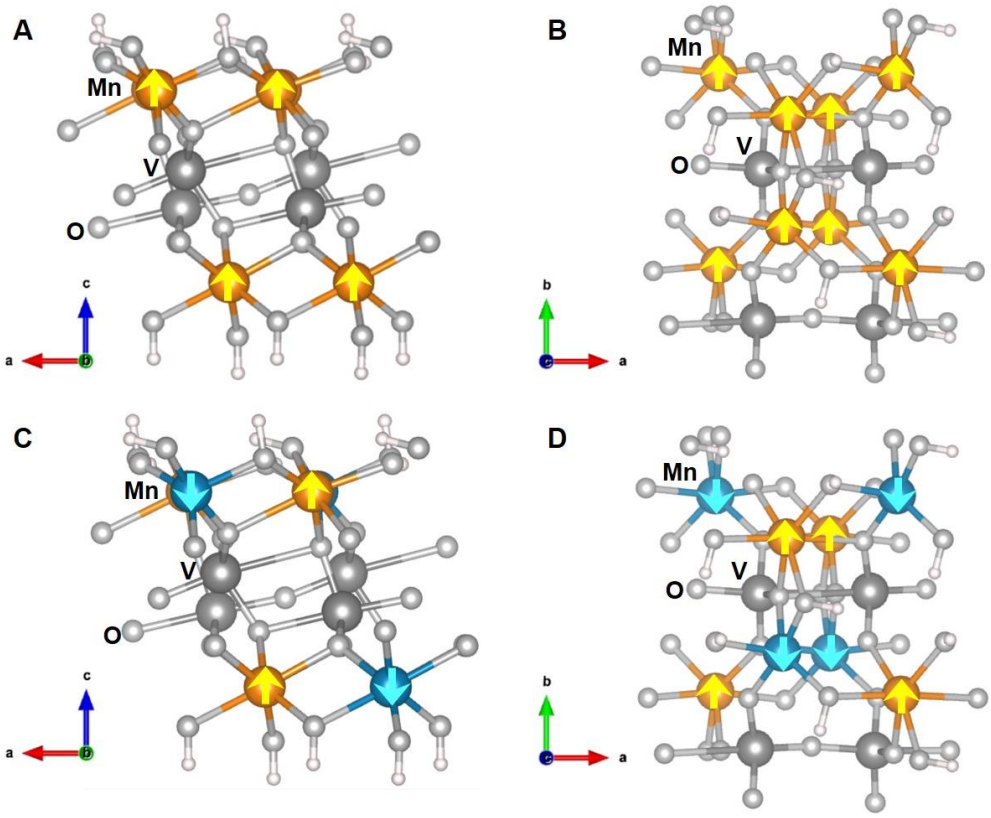

Fig. S16. Calculation models of $Mn_2V_2O_7$ (001) slab. A and **B**, Side-view and top-view of FM-$Mn_2V_2O_7$ (001) surface. **C** and **D**, Side-view and top-view of AFM-$Mn_2V_2O_7$ (001) surface.

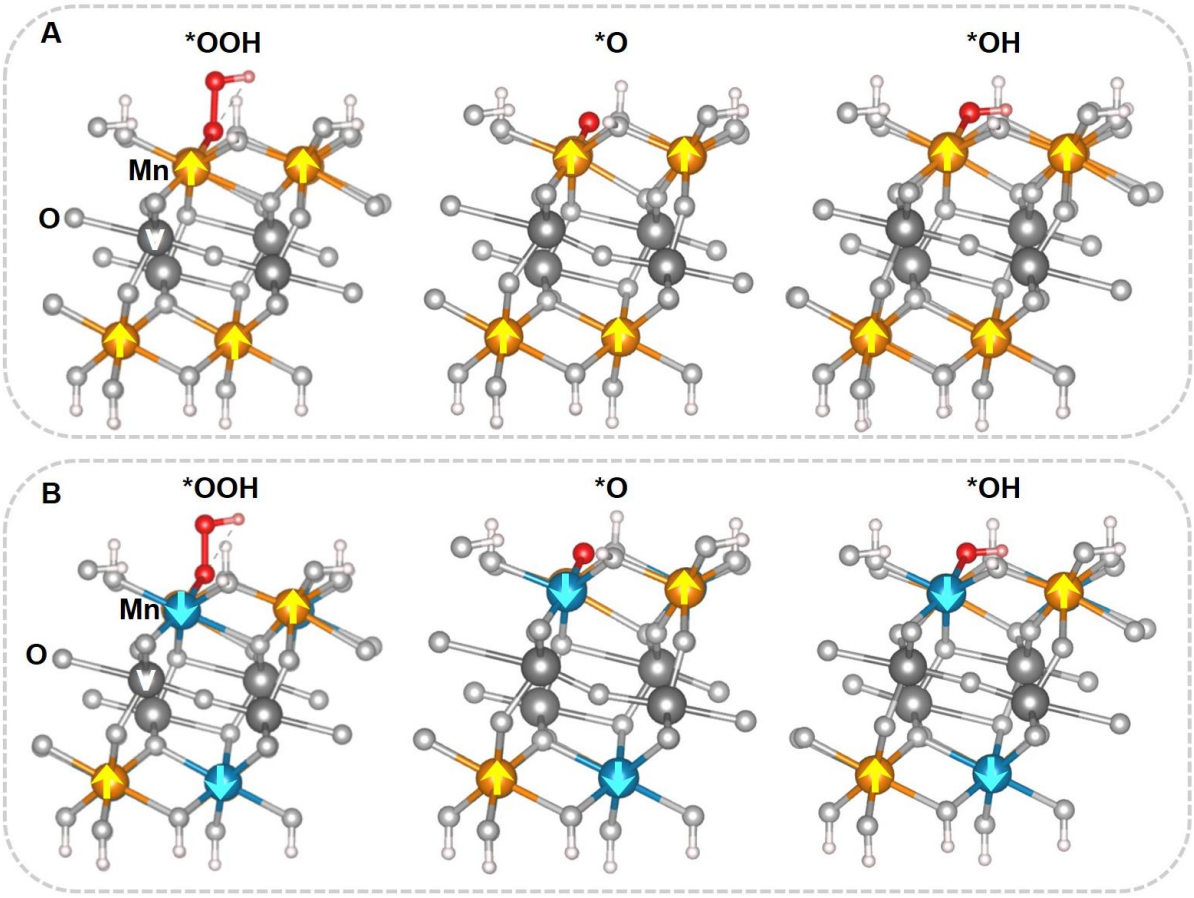

Fig. S17. Atomic configurations of *OOH, *O and *OH intermediates adsorbed on the surface of (**A**) FM- and (**B**) AFM-$Mn_2V_2O_7$, respectively.

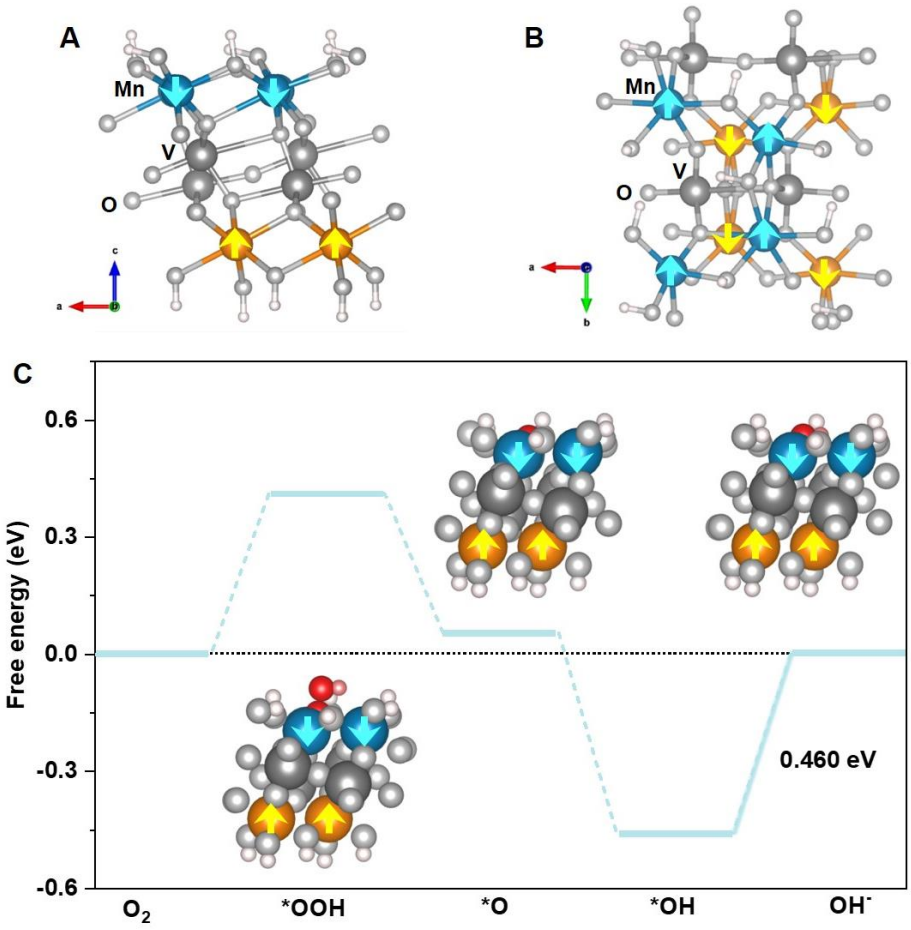

Fig. S18. DFT calculations of AFM-interlayer $Mn_2V_2O_7$. A and **B**, Side-view and top-view of $Mn_2V_2O_7$ (001) surface with interlayer AFM ordering. **C**, ORR free-energy diagram on $Mn_2V_2O_7$ (001) surface with interlayer AFM ordering at 1.23 V_{RHE}, with the inset showing atomic configurations of *OOH, *O and *OH intermediates adsorbed on $Mn_2V_2O_7$ (001) surface with interlayer AFM ordering. The highlight indicates the potential-limiting step. As seen in **C**, the potential-limiting step of AFM-interlayer $Mn_2V_2O_7$ is *OH desorption and the overpotential is 0.46 eV, which is similar to the case of FM-$Mn_2V_2O_7$ (Fig. 4*A*). This result is consistent with the energy calculation that AFM-interlayer $Mn_2V_2O_7$ is FM-$Mn_2V_2O_7$ like because the non-magnetic [VO_n] layer weakens the magnetic interaction between the neighbouring [MnO_6] layers (Note S2). Based on the results shown here and in the main text (Fig. 4), it is concluded that the ORR thermodynamics of $Mn_2V_2O_7$ is mainly governed by the magnetic interactions of neighbouring Mn atoms in the same [MnO_6] layer.

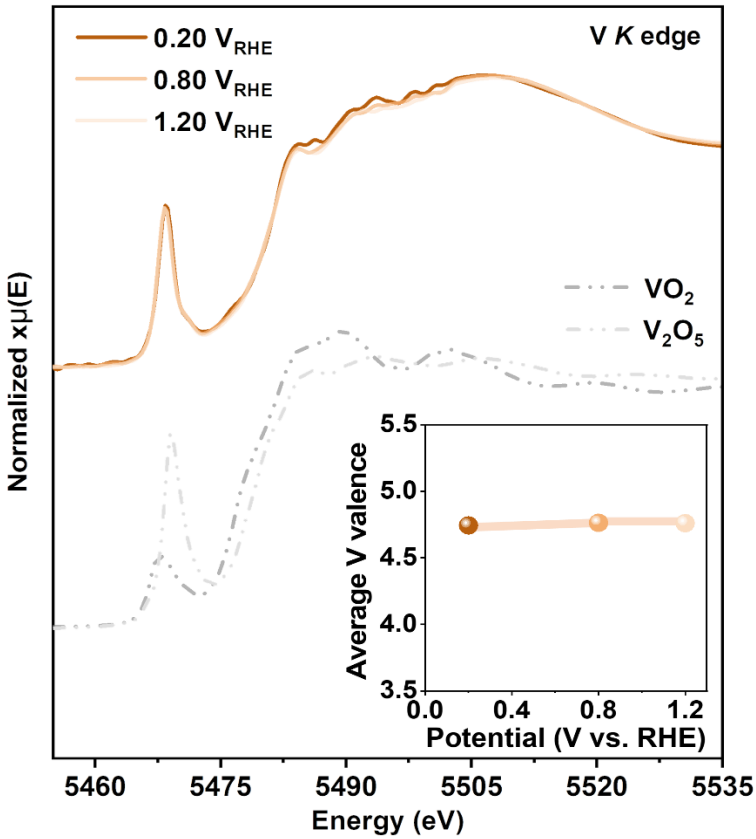

Fig. S19. *In situ* V *K*-edge XANES spectra of FM-$Mn_2V_2O_7$ at different applied potentials, with the inset showing the fitted V valence states in the range of 0.20~1.20 V_{RHE}. As shown, the V valence state does not change obviously with the applied potential, indicating that V ions in FM-$Mn_2V_2O_7$ are not the active sites for ORR.

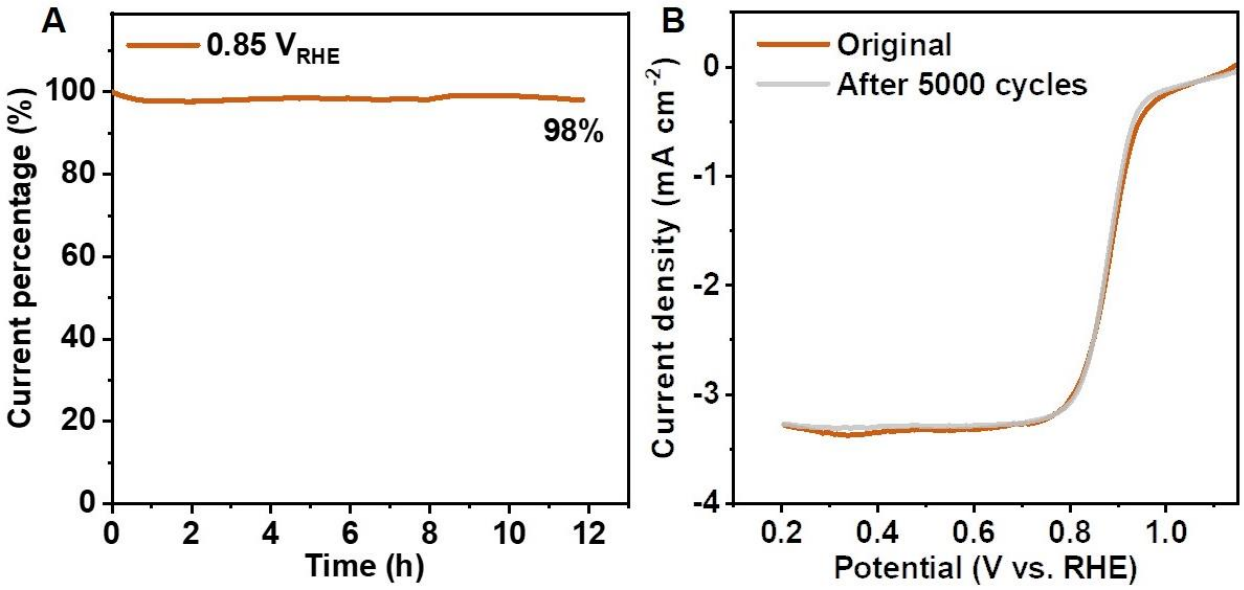

Fig. S20. Stability tests of FM-$Mn_2V_2O_7$. A, Chronoamperometric response of FM-$Mn_2V_2O_7$ at 0.85 V_{RHE}. **B**, ORR polarization curves of FM-$Mn_2V_2O_7$ before and after 5000 cyclic tests. As shown in **A**, FM-$Mn_2V_2O_7$ retained 98% of its initial current after 12 h continuous test. Moreover, there was no obvious negative shift of the polarization curve after 5000 continuous cycles (**B**). These collective results indicate that FM-$Mn_2V_2O_7$ possesses excellent ORR stability.

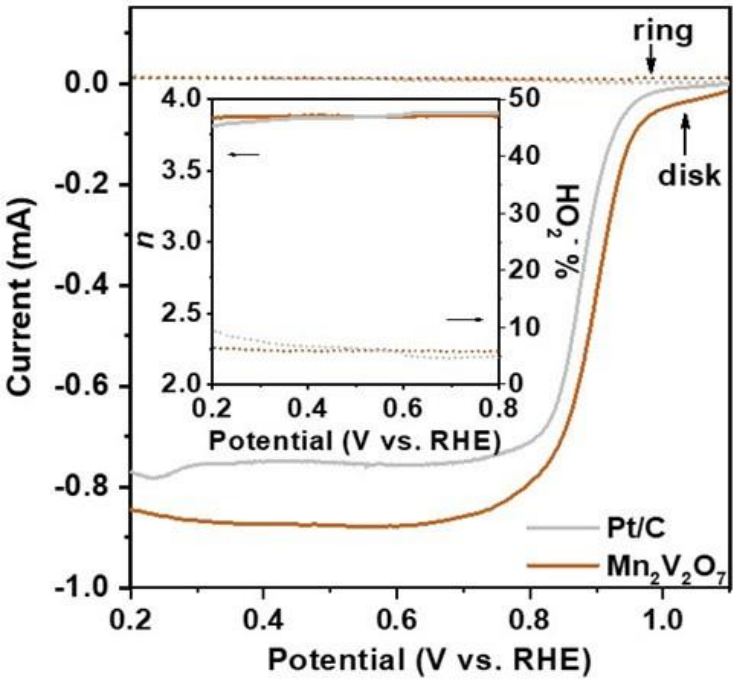

Fig. S21. RRDE voltammograms of FM-$Mn_2V_2O_7$ and Pt/C at 1600 rpm. The inset shows electron transfer number (*n*, solid line) and percentage of peroxide (HO_2^-%, dotted line) of FM-$Mn_2V_2O_7$ and Pt/C at various potentials based on the RRDE data. As shown, FM-$Mn_2V_2O_7$ prefers a 4-electron oxygen reduction pathway with a complete conversion of O_2 to H_2O, which is analogous to that observed on the Pt/C catalyst.

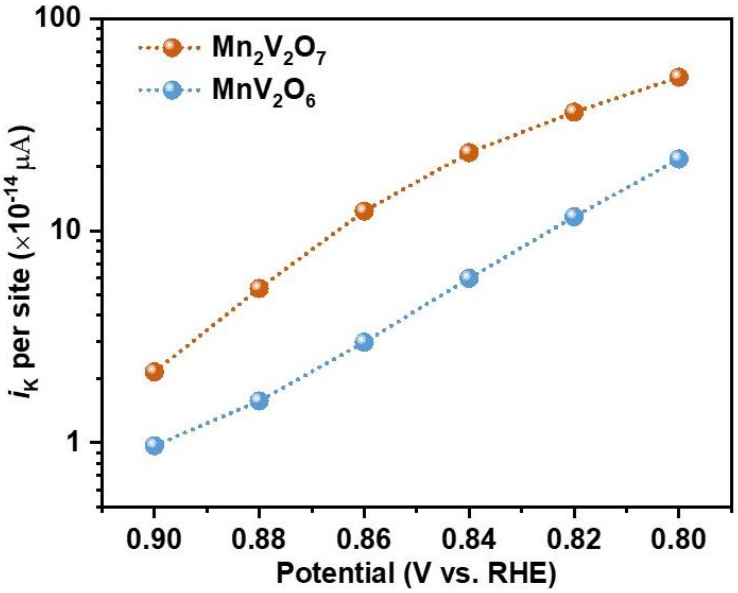

Fig. S22. Kinetic current per Mn site (i_K per site) for $Mn_2V_2O_7$ and MnV_2O_6 at various potentials.

To evaluate the intrinsic activity of FM-$Mn_2V_2O_7$ and AFM-MnV_2O_6, the kinetic currents were normalized to the total numbers of active Mn sites. Note that the total numbers of active Mn sites were obtained from CV fitting method. As shown, the value of i_K per site on FM-$Mn_2V_2O_7$ is 2 ~ 4 times larger than that on AFM-MnV_2O_6, suggesting that FM ordering improves the intrinsic activity of $Mn_2V_2O_7$, which is consistent with the DFT calculations (Fig. 4).

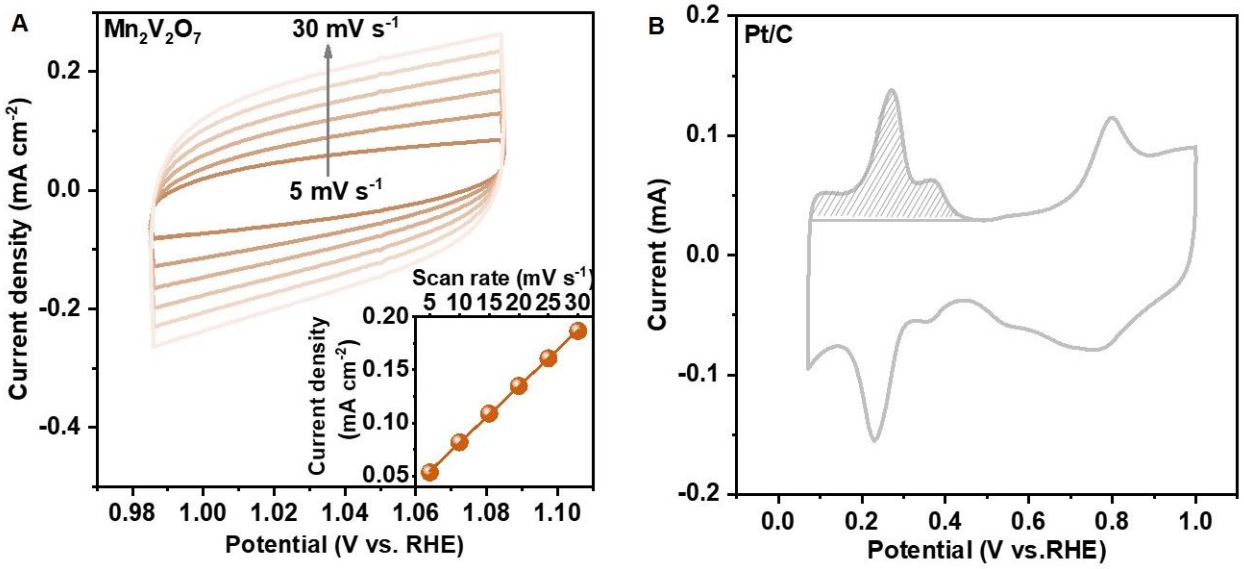

Fig. S23. Determination the ECSAs of FM-$Mn_2V_2O_7$ and Pt/C catalysts. A, CV curves of $Mn_2V_2O_7$ at scan rates from 5 to 30 mV s^{-1}, with the inset showing current density measured at 1.035 V_{RHE} plotted as a function of scan rate to determine the ECSA of $Mn_2V_2O_7$. **B**, CV curve of Pt/C in N_2-saturated 1.0 M KOH with a scan rate of 50 mV s^{-1} to determine its ECSA.

The ECSA of $Mn_2V_2O_7$ was calculated by the equation (10):

$$\text{ECSA}=\frac{R_f}{m_{loading}} \tag{S2}$$

$$R_f = \frac{C_{dl}}{C_s} \tag{S3}$$

where R_f is the roughness factor of catalyst, $m_{loading}$ =0.5 mg cm^{-2} is the mass-loading of $Mn_2V_2O_7$, C_{dl} is the double-layer capacitance obtained from the inset of (a), and C_s is the specific capacitance of 60 μF cm^{-2} for oxide (4). The calculated ECSA for $Mn_2V_2O_7$ catalyst was 17.7 m^2 g^{-1}.

The ECSA of Pt/C was calculated by the equation:

$$\text{ECSA} = \frac{Q_H}{Q_S \cdot m_{Pt}} \tag{S4}$$

where Q_H is coulombic charge that can be calculated by integrating the area of the H_{upd} adsorption/desorption region, Q_S is specific charge assuming the value of 0.21 mC cm^{-2} for the adsorption of a hydrogen monolayer, and m_{Pt} is the loading mass of Pt. The calculated ECSA for Pt/C catalyst was 51.7 m^2 g^{-1}, that is close to the value in the literature (11).

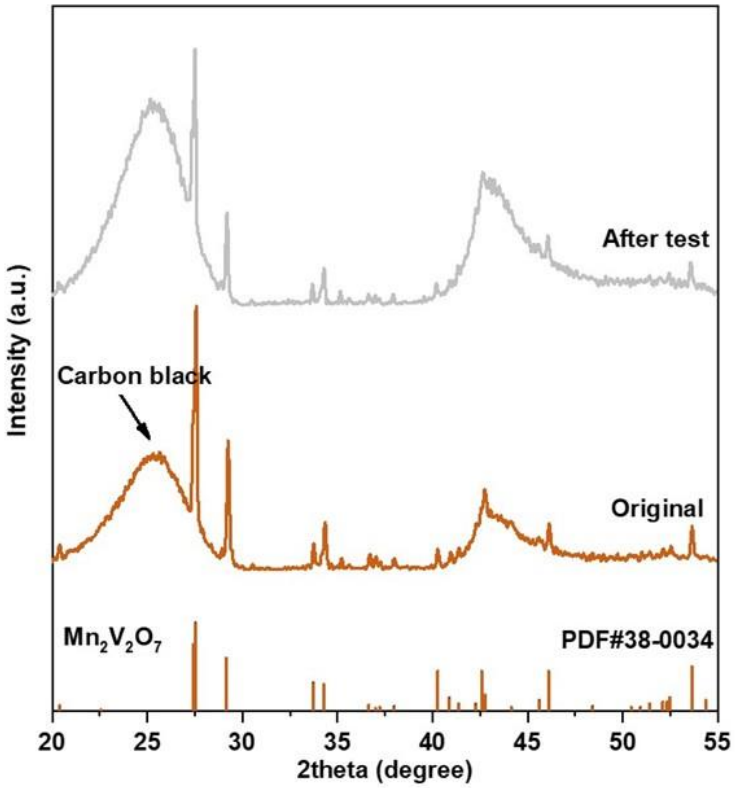

Fig. S24. XRD patterns of FM-$Mn_2V_2O_7$ before and after cyclic testing. As shown, following the cyclic test, the crystal structure of FM-$Mn_2V_2O_7$ remained intact.

Fig. S25. Photograph of the experimental setup for electrochemical testing under an external magnetic field.

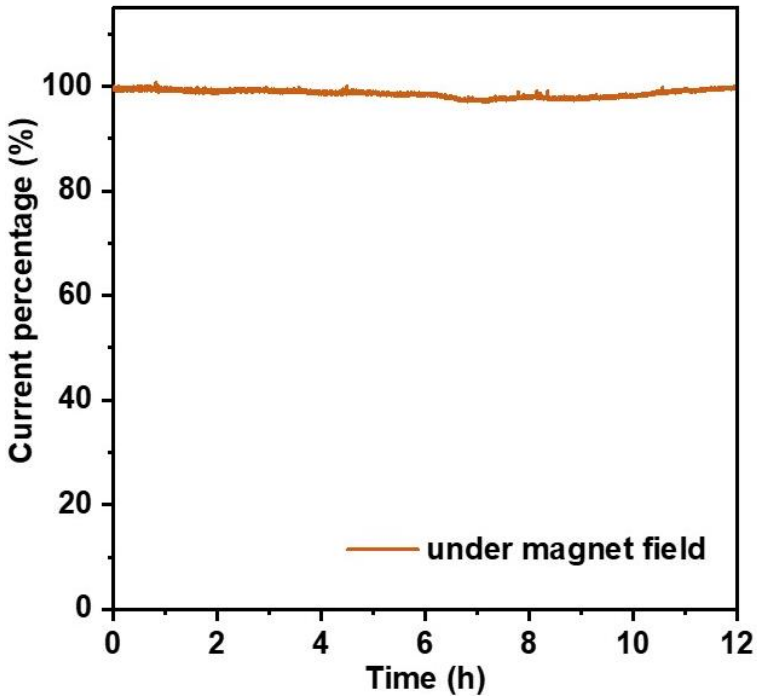

Fig. S26. Chronoamperometric response of FM-$Mn_2V_2O_7$ at 0.85 V_{RHE} under magnetic field. As shown, FM-$Mn_2V_2O_7$ exhibits negligible ORR current loss after 12 h continuous test, showing its excellent stability under magnetic field.

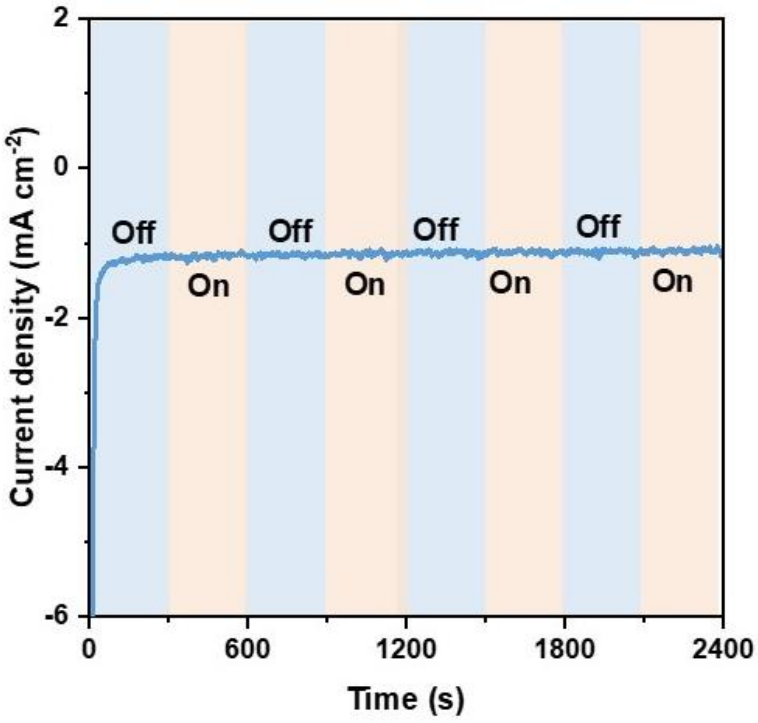

Fig. S27. Magneto-chronoamperometry experiment of AFM-MnV_2O_6 in O_2-saturated 1.0 M KOH at 0.78 V_{RHE}. As seen, AFM-MnV_2O_6 exhibits no obvious response under the external magnetic field.

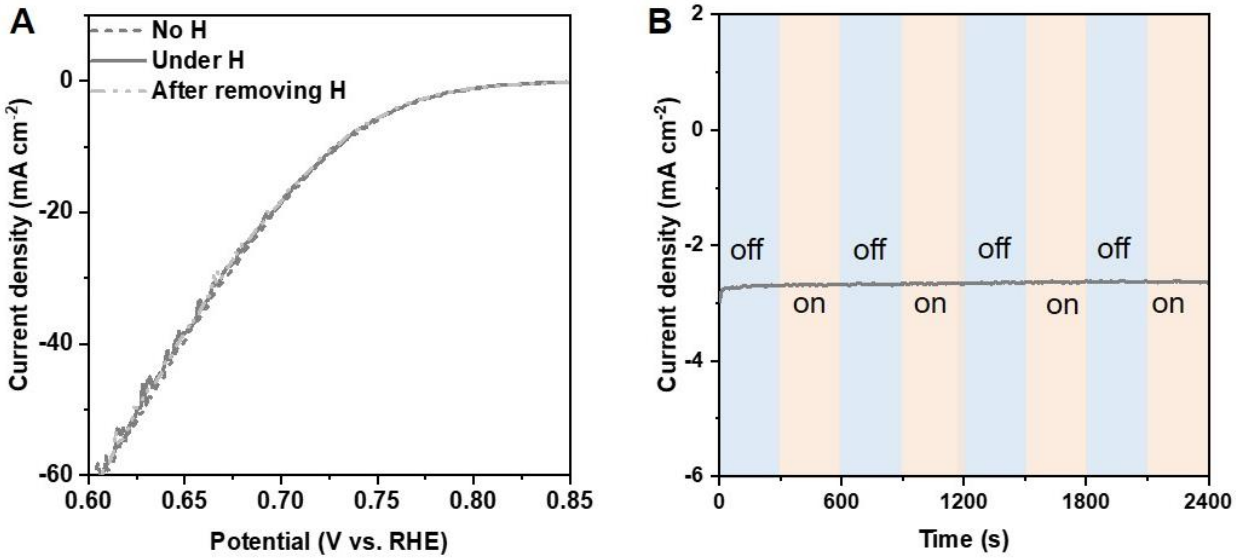

Fig. S28. Magnetic field response of Pt/C. A, LSV curves of Pt/C in O_2-saturated 1.0 M KOH at a scan rate of 5 mV s^{-1} with no magnetic field (H), under magnetic field, and after removing magnetic field (~ 1 T). **B**, Magneto-chronoamperometry experiment of Pt/C in O_2-saturated 1.0 M KOH at 0.78 V_{RHE}. As seen, the Pt/C catalyst exhibits no obvious response under the external magnetic field.

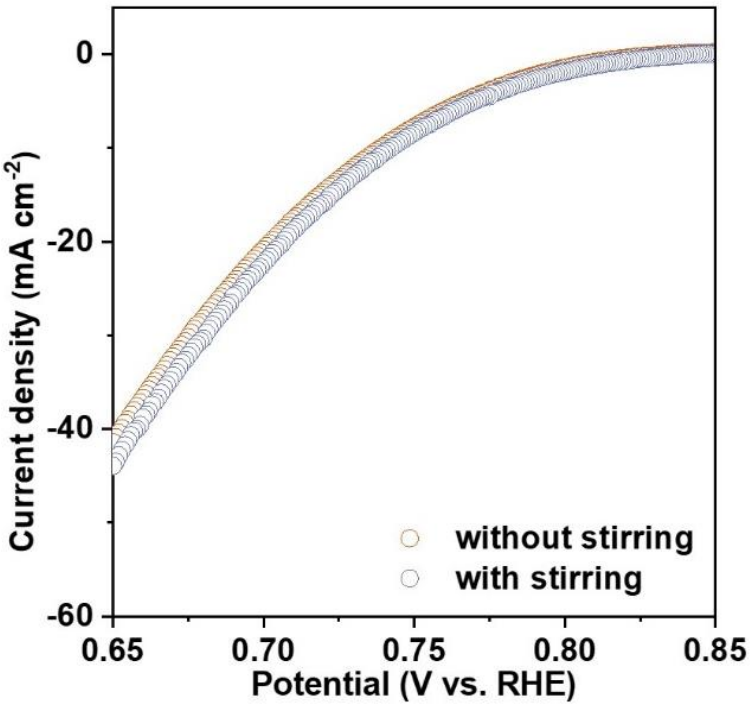

Fig. S29. LSV curves of $Mn_2V_2O_7$ in O_2-saturated 1.0 M KOH at a scan rate of 5 mV s^{-1} without and with stirring.

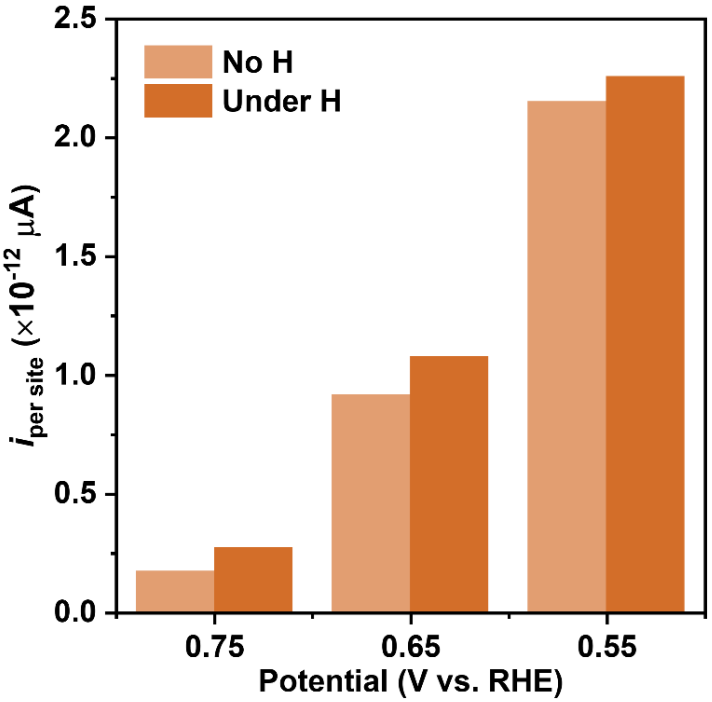

Fig. S30. ORR current of per Mn^{3+} site ($i_{per\ site}$) on FM-$Mn_2V_2O_7$ at various potentials with no magnetic field and under magnetic field. Here, $i_{per\ site}$ was calculated by normalizing the current to the number of active Mn^{3+} ions (shown in Table S2). As shown, the $i_{per\ site}$ of Mn^{3+} site on FM-$Mn_2V_2O_7$ under magnetic field is higher than that with no magnetic field at a certain potential, confirming that the magnetic field enhances the intrinsic activity of each Mn^{3+} site on FM-$Mn_2V_2O_7$.

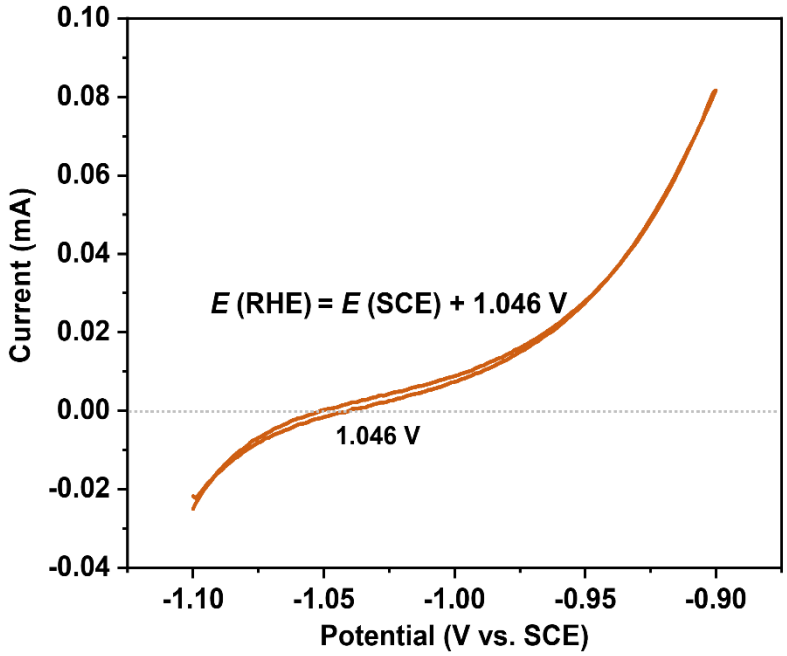

Fig. S31. Calibration of reference saturated calomel electrode (SCE) in 1.0 M KOH. The reference SCE was calibrated with respect to reversible hydrogen electrode (RHE). The calibration was performed in a high-purity H_2-saturated electrolyte with a Pt electrode as the working electrode. The scanning rate of CV was 1 mV s^{-1}, and the average value of the two potentials with zero current was taken as the thermodynamic potential (12). Therefore, in 1.0 M KOH, *E* (RHE) = *E* (SCE) + 1.046 V.

Supplementary Tables

Table S1. The calculated total oxygen magnetic moments of $Mn_2V_2O_7$ and MnV_2O_6 with FM and AFM orderings.

Model	Magnetic moment of O atom (μ_B)
FM-$Mn_2V_2O_7$	-0.212
AFM-$Mn_2V_2O_7$	0
FM-MnV_2O_6	-0.928
AFM-MnV_2O_6	0

Table S2. Calculated site density of Mn ions on FM-$Mn_2V_2O_7$ and AFM-MnV_2O_6 by the CV fitting method.

Samples	Mn^{3+} density ($\times 10^{15}$ cm^{-2})
FM-$Mn_2V_2O_7$	45.165
AFM-MnV_2O_6	7.889
FM-$Mn_2V_2O_7$-under H	50.163

Table S3. Comparison of CV fitting and XPS results of FM-$Mn_2V_2O_7$ and AFM-MnV_2O_6.

Samples	Number ratio of Mn^{3+}/Mn^{4+} by CV analysis	Number ratio of Mn^{3+}/Mn^{4+} by XPS analysis[a]
FM-$Mn_2V_2O_7$	1.0	1.0
AFM-MnV_2O_6	1.7	1.8

[a]obtained from Table S5

Table S4. Evaluation of Mn valence states of FM-$Mn_2V_2O_7$ at different applied potentials by the LCF analysis.

Potential (V_{RHE})	Relative content (%)				Mn valence state
	MnO	Mn_3O_4	Mn_2O_3	MnO_2	
Initial	86.5	13.5	--	--	2.09
0.20	43.0	57.0	--	--	2.38
0.40	19.2	80.8	--	--	2.54
0.60	19.7	78.9	1.4	--	2.54
0.80	--	30.3	51.2	18.5	3.08
1.20	--	29.9	24.9	45.3	3.36

Table S5. Comparison of Mn valence states of FM-$Mn_2V_2O_7$ and AFM-MnV_2O_6 after testing at 1.20 V_{RHE} based on XPS analysis.

Samples	Relative content (%)			Mn valence state
	Mn^{2+}	Mn^{3+}	Mn^{4+}	
FM-$Mn_2V_2O_7$	6.7	47.0	46.3	3.40
AFM-MnV_2O_6	46.8	34.5	18.7	2.72

Table S6. DFT calculated energy difference (ΔE) between FM- and AFM-$Mn_2V_2O_7$.

Model	ΔE (meV)
FM-$Mn_2V_2O_7$	0
AFM-$Mn_2V_2O_7$	47.17

Table S7. DFT calculated energy difference (ΔE) per primitive cell between AFM ordered and FM ordered $Mn_2V_2O_7$.

Model	ΔE (meV)
AFM-$Mn_2V_2O_7$	23.58[a]
AFM-interlayer $Mn_2V_2O_7$	**5.59**[b]

[a] $\Delta \boldsymbol{E}_{\text{AFM-}Mn_2V_2O_7} = \boldsymbol{E}_{\text{AFM-}Mn_2V_2O_7} - \boldsymbol{E}_{\text{FM-}Mn_2V_2O_7}$

[b] $\Delta \boldsymbol{E}_{\text{AFM-interlayer }Mn_2V_2O_7} = \boldsymbol{E}_{\text{AFM-interlayer }Mn_2V_2O_7} - \boldsymbol{E}_{\text{FM-}Mn_2V_2O_7}$

Table S8. Bader charge analysis of Mn site on the surface of Mn oxides.

Sample	Mn valence state	Bader charge (|e|)
$Mn_2V_2O_7$ (001)	+3	-1.745
MnO-bulk	+2	-1.413
Mn_3O_4-bulk	+2, +3	-1.479, -1.695
Mn_2O_3-bulk	+3	-1.729
MnO_2-bulk	+4	-1.862

Table S9. Zero-point energy (*ZPE*) and entropy (*S*) corrections of reaction intermediate species.

Species	Energy (eV)	*ZPE* (eV)	*TS* (eV)
H_2O	-14.22	0.57	0.67
H_2	-6.77	0.27	0.40
*OOH	-18.29	0.73	0.73
*OH	-10.84	0.43	0.47
*O	-7.45	0.30	0.27

Table S10. Summary of the recently reported highly active ORR oxide catalysts in alkaline solutions.

Catalyst	E_{onset} (V)	$E_{1/2}$ (V)	i_s (μA cm^{-2})	Electrolyte	Surface area (m^2 g^{-1})	Reference
FM-$Mn_2V_2O_7$	**0.97**	**0.89**	**74 @ 0.90 V**	**1.0 M KOH**	**24.12**	**This work**
$Mg_xCo_{3-x}O_4$	0.95	0.839	--	0.1 M KOH	245.5	(13)
$MnCo_2O_4$	0.92	0.78	--	0.1 M KOH	16.07	(14)
CoO	--	0.849	--	0.1 M KOH	183.1	(15)
Mo_1/La_2CoMnO_6[a]	--	--	25 @ 0.99 V	0.1 M KOH	1.25	(16)
$Mn_{1.5}Co_{1.5}O_4$	--	0.82	--	0.1 M KOH	--	(17)
$ZnCo_{1.4}Mn_{0.6}O_4$	--	0.81	--	0.1 M KOH	25	(18)
CoV_2O_4	0.91	0.83	37 @ 0.85 V	1.0 M KOH	14	(19)
$Mn_{0.8}(CoFe_2)_{0.73}O_4$	--	0.89	--	1.0 M NaOH	--	(20)
CoO	0.96	0.85	144 @ 0.60 V	1.0 M KOH	27	(21)
$SmMn_2O_{5-\delta}$	0.96	0.77	23 @ 0.80 V 123 @ 0.70 V	0.1 M KOH	57	(22)
$La_2CoMnO_{6-\delta}$	0.92	0.75	--	0.1 M KOH	--	(23)
$La_2NiMnO_{6-\delta}$	0.91	0.70	--	0.1 M KOH	--	(23)
Mn_3O_4	0.87	0.65	--	0.1 M KOH	--	(24)
$(La_{0.8}Sr_{0.2})_{0.95}Mn_{0.95}Ir_{0.05}O_3$	0.92	--	--	0.1 M KOH	26	(25)
$LaMn_{0.3}Co_{0.7}O_3$	--	0.72	--	0.1 M KOH	59	(26)

[a]atomically dispersed Mo^{6+} modified La_2CoMnO_6

SI References

1. Q. Yan, G. Li, P. F. Newhouse, J. Yu, K. A. Persson, J. M. Gregoire, J. B. Neaton, $Mn_2V_2O_7$: An earth abundant light absorber for solar water splitting. *Adv. Energy Mater.* 5, 1401840 (2015).
2. K. A. Persson, B. Waldwick, P. Lazic, G. Ceder, Prediction of solid-aqueous equilibria: Scheme to combine first-principles calculations of solids with experimental aqueous states. *Phys. Rev. B* 85, 235438 (2012).
3. J. Rossmeisl, J. K. Nørskov, C. D. Taylor, M. J. Janik, M. Neurock, Calculated phase diagrams for the electrochemical oxidation and reduction of water over Pt(111). *J. Phys. Chem. B* 110, 21833−21839 (2006).
4. C Wei, S. Sun, D. Mandler, X. Wang, S. Z. Qiao, Z. J. Xu. Approaches for measuring the surface areas of metal oxide electrocatalysts for determining their intrinsic electrocatalytic activity. *Chem. Soc. Rev.* 48, 2518−2534 (2019).
5. W. C. Sheng, H. A. Gasteiger, Y. Shao-Horn, Hydrogen oxidation and evolution reaction kinetics on platinum: acid vs alkaline electrolytes. *J. Electrochem. Soc.* 157, 1529−1536 (2010).
6. R. P. Forslund, W. G. Hardin, X. Rong, A. M. Abakumov, D. Filimonov, C. T. Alexander, J. T. Mefford, H. Iyer, A. M. Kolpak, K. P. Johnston, K. J. Stevenson, Exceptional electrocatalytic oxygen evolution via tunable charge transfer interactions in $La_{0.5}Sr_{1.5}Ni_{1-x}Fe_xO_{4\pm\delta}$ Ruddlesden-Popper oxides. *Nat. Commun.* 9, 3150 (2018).
7. Y. Yang, Y. Wang, Y. Xiong, X. Huang, L. Shen, R. Huang, H. Wang, J. P. Pastore, S. H. Yu, L. Xiao, J. D. Brock, L. Zhuang, H. D. Abruna, *In situ* X-ray absorption spectroscopy of a synergistic Co-Mn oxide catalyst for the oxygen reduction reaction. *J. Am. Chem. Soc.* 141, 1463−1466 (2019).
8. J. Suntivich, H. A. Gasteiger; N. Yabuuchi; Y. Shao-Horn, Electrocatalytic measurement methodology of oxide catalysts using a thin-film rotating disk electrode. *J. Electrochem. Soc.* 157, 1263−1268 (2010).
9. D.-G. Lee, O. Gwon, H.-S. Park, S. H. Kim, J. Yang, S. K. Kwak, G. Kim, H.-K. Song, Conductivity-dependent completion of oxygen reduction on oxide catalysts. *Angew. Chem. Int. Ed.* 54, 15730−15733 (2015).
10. Y. J. Li, L. Cui, P. F. Da, K. W. Qiu, W. J. Qin, W. B. Hu, X. W. Du, K. Davey, T. Ling, S. Z. Qiao, Multiscale structural engineering of Ni-doped CoO nanosheets for zinc-air batteries with high power density. *Adv. Mater.* 30, 1804653 (2018).
11. H. Yin, S. Zhao, K. Zhao, A. Muqsit, H. Tang, L. Chang, H. Zhao, Y. Gao, Z. Tang, Ultrathin platinum nanowires grown on single-layered nickel hydroxide with high hydrogen evolution activity. *Nat. Commun.* 6, 6430 (2015).
12. Y. Liang, Y. Li, H. Wang, J. Zhou, J. Wang, T. Regier, H. Dai, Co_3O_4 nanocrystals on graphene as a synergistic catalyst for oxygen reduction reaction. *Nat. Mater.* 10, 780−786 (2011).
13. Y. Zhang, Z. Zhang, G. Jiang, A. H. Mamaghani, S. Sy, R. Gao, Y. Jiang, Y. Deng, Z. Bai, L. Yang, A. Yu, Z. Chen, Three-dimensionally ordered mesoporous Co_3O_4 decorated with Mg as bifunctional oxygen electrocatalysts for high-performance zinc-air batteries. *Nano Energy* 100, 107425 (2022).
14. L. An, Y. Hu, J. Li, J. Zhu, M. Sun, B. Huang, P. Xi, C. H. Yan, Tailoring oxygen reduction reaction pathway on spinel oxides via surficial geometrical-site occupation modification driven by the oxygen evolution reaction. *Adv. Mater*. 34, 2202874 (2022).
15. Y. Tian, X. Liu, L. Xu, D. Yuan, Y. Dou, J. Qiu, H. Li, J. Ma, Y. Wang, D. Su, S. Zhang, Engineering crystallinity and oxygen vacancies of Co(II) oxide nanosheets for high performance and robust rechargeable Zn-air batteries. *Adv. Funct. Mater.* 31, 2101239 (2021).
16. Z. Zhuang, Y. Li, Y. Li, J. Huang, B. Wei, R. Sun, Y. Ren, J. Ding, J. Zhu, Z. Lang, L. V. Moskaleva, C. He, Y. Wang, Z. Wang, D. Wang, Y. Li, Atomically dispersed nonmagnetic electron traps improve oxygen reduction activity of perovskite oxides. *Energy Environ. Sci.* 14, 1016−1028 (2021).

17. K. Li, R. Zhang, R. Gao, G.-Q. Shen, L. Pan, Y. Yao, K. Yu, X. Zhang, J.-J. Zou, Metal-defected spinel $Mn_xCo_{3-x}O_4$ with octahedral Mn-enriched surface for highly efficient oxygen reduction reaction. *Appl. Catal. B. Environ.* 244, 536−545 (2019).
18. Y. Zhou, S. Sun, S. Xi, Y. Duan, T. Sritharan, Y. Du, Z. J. Xu, Superexchange effects on oxygen reduction activity of edge-sharing $[Co_xMn_{1-x}O_6]$ octahedra in spinel oxide. *Adv. Mater.* 30, 1705407 (2018).
19. C. Mu, J. Mao, J. Guo, Q. Guo, Z. Li, W. Qin, Z. Hu, K. Davey, T. Ling, S. Z. Qiao, Rational design of spinel cobalt vanadate oxide Co_2VO_4 for superior electrocatalysis. *Adv. Mater.* 32, 1907168 (2020).
20. Y. Xiong, Y. Yang, X. Feng, F. J. DiSalvo, H. D. Abruña, A strategy for increasing the efficiency of the oxygen reduction reaction in Mn-doped cobalt ferrites. *J. Am. Chem. Soc.* 141, 4412−4421 (2019).
21. T. Ling, D. Y. Yan, Y. Jiao, H. Wang, Y. Zheng, X. Zheng, J. Mao, X. W. Du, Z. Hu, M. Jaroniec, S. Z. Qiao, Engineering surface atomic structure of single-crystal cobalt (II) oxide nanorods for superior electrocatalysis. *Nat. Commun.* 7, 12876 (2016).
22. C. Dong, Z. W. Liu, J. Y. Liu, W. C. Wang, L. Cui, R. C. Luo, H. L. Guo, X. L. Zheng, S. Z. Qiao, X. W. Du, J. Yang, Modest oxygen-defective amorphous manganese-based nanoparticle mullite with superior overall electrocatalytic performance for oxygen reduction reaction. *Small* 13, 1603903 (2017).
23. M. Jiang, J. Li, Y. Zhao, L. Pan, Q. Cao, D. Wang, Y. Du, Double perovskites as model bifunctional catalysts toward rational design: The correlation between electrocatalytic activity and complex spin configuration. *ACS Appl. Mater. Interfaces* 10, 19746−19754 (2018).
24. Y.-C. Zhang, S. Ullah, R. Zhang, L. Pan, X. Zhang, J.-J. Zou, Manipulating electronic delocalization of Mn_3O_4 by manganese defects for oxygen reduction reaction. *Appl. Catal. B Environ.* 277, 119247 (2020).
25. L. Yan, Y. Lin, X. Yu, W. Xu, T. Salas, H. Smallidge, M. Zhou, H. Luo, $La_{0.8}Sr_{0.2}MnO_3$-based perovskite nanoparticles with the A-site deficiency as high performance bifunctional oxygen catalyst in alkaline solution. *ACS Appl. Mater. Interfaces* 9, 23820−23827 (2017).
26. J. Sun, L. Du, B. Sun, G. Han, Y. Ma, J. Wang, H. Huo, C. Du, G. Yin, Bifunctional $LaMn_{0.3}Co_{0.7}O_3$ perovskite oxide catalyst for oxygen reduction and evolution reactions: The optimized e_g electronic structures by manganese dopant. *ACS Appl. Mater. Interfaces* 12, 24717−24725 (2020).